

The G 305 Star-forming Region: II. Irregular variable stars.

N. MEDINA,^{1,2} J. BORISSOVA,^{1,2} R. KURTEV,^{1,2} J. ALONSO-GARCÍA,^{3,2} CARLOS G. ROMÁN-ZÚÑIGA,⁴ A. BAYO,^{1,5}
MARINA KOUNKEL,⁶ ALEXANDRE ROMAN-LOPES,⁷ P. W. LUCAS,⁸ K. R. COVEY,⁹ FRANCISCO FÓRSTER,^{10,11}
DANTE MINNITI,¹² LUCIA ADAME,⁴ AND JESÚS HERNÁNDEZ⁴

¹*Instituto de Física y Astronomía, Universidad de Valparaíso, Av. Gran Bretaña 1111, Playa Ancha, Casilla 5030, Chile.*

²*Millennium Institute of Astrophysics, Nuncio Monsenor Sotero Sanz 100, Of. 104, Providencia, Santiago, Chile.*

³*Centro de Astronomía (CITEVA), Universidad de Antofagasta, Av. Angamos 601, Antofagasta, Chile.*

⁴*Universidad Nacional Autónoma de México, Instituto de Astronomía, AP 106, Ensenada 22800, BC, Mexico*

⁵*Núcleo Milenio Formación Planetaria - NPF, Universidad de Valparaíso, Av. Gran Bretaña 1111, Valparaíso, Chile.*

⁶*Department of Physics and Astronomy, Western Washington University, 516 High St., Bellingham, WA 98225, USA*

⁷*Departamento de Astronomía, Universidad de La Serena, Av. Cisternas 1200N, La Serena, Chile*

⁸*Centre for Astrophysics, University of Hertfordshire, College Lane, Hatfield, AL10 9AB, UK.*

⁹*Department of Physics and Astronomy, Western Washington University, Bellingham, USA*

¹⁰*Center for Mathematical Modeling, University of Chile, AFB170001, Chile*

¹¹*Millennium Institute of Astrophysics (MAS), Santiago, Chile.*

¹²*Departamento de Física, Facultad de Ciencias Exactas, Universidad Andrés Bello, Av. Fernandez Concha 700, Las Condes, Santiago, Chile.*

(Received; Revised; Accepted)

Submitted to AJ

ABSTRACT

We present a catalog of 167 newly discovered, irregular variables spanning a ~ 7 deg² area that encompasses the G 305 star-forming complex, one of the most luminous giant HII regions in the Galaxy. We aim to unveil and characterize the young stellar object (YSO) population of the region by analyzing the K_s -band variability and JHK_s infrared colors from the *VISTA Variables in the Vía Láctea* (VVV) survey. Additionally, SDSS-IV APOGEE-2 infrared spectra of selected objects are analyzed.

The sample show relatively high amplitudes ($0.661 < \Delta K_S < 3.521$ mag). Most of them resemble sources with outbursts with amplitude > 1 mag and duration longer than a few days, typically at least a year, known as *Eruptive Variables*. About 60% are likely to be Class II/Flat/I objects. This is also confirmed by the spectral index α when available.

From the analysis of APOGEE-2 near-infrared spectra of sources in the region, another 122 stars are classified as YSOs, and displays some infrared variability. The measured effective temperature T_{eff} peak is around 4000K and they are slightly super-solar in metal abundance. The modal radial velocity is approximately -41 km/s.

Combining available catalogs of YSOs in the region with our data, we investigate the spatial distributions of 700 YSOs. They are clearly concentrated within the central cavity formed by the massive clusters Danks 1 and 2. The calculated surface density for the entire catalog is 0.025 YSOs/pc⁻², while the central cavity contains 10 times more objects per area (0.238 YSOs/pc⁻²).

Keywords: — infrared: stars — stars: pre-main sequence — stars: variables: general — (Galaxy:) open clusters and associations: general — (Galaxy:) open clusters and associations: individual (G305)

1. INTRODUCTION

Since stars in formation or in very early stages of evolution undergo rapid structural changes, variations in their luminosity and colours are widely observed. Historically, various types of brightness changes have been noticed in young stellar objects (YSOs). For instance, strong variability may be due to accretion events, while smaller-scale variability may be caused by geometrical effects, such as clearing of dust, spots, and rotation (Audard et al. 2014). FU Orionis stars (FUors; Herbig 1966) are thought to be pre-main sequence (pre-MS) stars characterized by increases in brightness by > 4 magnitudes in optical wavelengths. According to Audard et al. (2014), only about two dozen such sources were known in 2014. EX Lupi-type objects (EXors; Herbig 1989) show similar brightness increases to FUors, but with shorter timescales. There are still problems in the interpretation of the variety of outburst intensities and timescales for those types of stars.

This variable brightness also can be observed in several stages of the classical model of pre-MS evolution, after the collapse of a molecular cloud has begun. Due to conservation of angular momentum, the infalling matter forms a protostellar disk, through which accretion on to the central source occurs (McKee & Ostriker 2007; Li et al. 2014). Numerous physical processes are involved in the evolution from a heavily obscured protostar until it reaches the main sequence. The physical origin of the variability could be a consequence of irregular intrinsic changes, such as episodic accretion (Audard et al. 2014), variable extinction induced by their circumstellar disks (e.g., Meyer et al. 1997; Cody et al. 2014; Rebull et al. 2014a), rotational modulation by cool and hot spots on the stellar surface, and the variations in accretion disk/envelope geometry. Massive YSOs, with $M > 7M_{\odot}$, likely undergo slightly different accretion and formation processes (Davies et al. 2011; Mottram et al. 2011; Frost et al. 2021). Observations of variability may provide some insight into these processes (Caratti o Garatti et al. 2017).

Rice et al. (2015) determined that the amplitude of brightness variations is correlated with evolutionary class in YSOs. In other words, Class I YSOs are more variable than Class II, which are in turn more variable than Class III. Therefore YSOs at earlier evolutionary stages will be preferentially identified in variability-based searches.

Optical variability was one of the original, defining characteristics of a YSO (Joy 1945; Herbig 1952). Therefore, in addition to analysis based on spectroscopy, the colour-magnitude diagram (CMD), and the colour-colour diagram (CCD), the study of photometric variability has been essential to understand the underlying physical processes. Existing time-domain surveys (e.g., the Catalina Real-time Transient Survey (Drake et al. 2009), the Pan-STARRS survey (Kaiser et al. 2002)), the near future Gaia variability releases (Gaia Collaboration et al. 2019) and the Vera C. Rubin Observatory, previously known as the Large Synoptic Survey Telescope (LSST; Ivezić et al. 2019) provide and will continue providing both large area and time-series covering in the optical wavelength regime.

However, the YSOs are often located inside or adjacent to dense molecular clouds (Evans et al. 2009) These clouds of material absorb and re-emit an important amount of the radiation from the young sources. Also, the disks and envelopes of the YSOs themselves are optically thick. Photometric surveys in the mid-infrared (MIR), such as Young Stellar Object VARIability (YSOVAR; Rebull et al. 2014b), or in the near-infrared (NIR) are very useful to minimize the influence of interstellar extinction. One of these NIR surveys is the *VISTA Variables in the Vía Láctea* survey (VVV; Minniti et al. 2010; Saito et al. 2012) and its undergoing extension, the *VISTA Variables in the Vía Láctea Extended* survey (VVVX; Minniti 2018). The VVV survey is fully comparable to the optical ones both in area and time-domain coverage (Arnaboldi et al. 2007) and have been designed to catalogue more than 10^9 sources, where 10^6 are expected to be variable stars. VVV is very suitable to characterize the changes along time. Several authors reported objects with considerable amplitudes (> 1 mag; Contreras Peña et al. 2017a) in K and K_S bands, and also revealing that variability in the NIR is relatively common in YSOs. According to Rice et al. (2012), out of the 30 YSOs they studied, 28 (93%) are variable. Figure 1 shows an example demonstrating a significant brightness change of the variable source named d084.v8, discovered in this work. The K_S images correspond to different epochs (marked in the top of each image).

1.1. The G 305 region

G 305 (Fig. 2) is one of the most massive star-forming regions in our Galaxy, located within the Scutum-Crux arm (in galactic coordinates: $l = 305.506^\circ$, $b = 00.085^\circ$). Its integrated radio luminosity can be directly comparable to the most luminous giant HII regions of the Galaxy (Conti & Crowther 2004). G 305 is also a valuable laboratory for studying sequential star formation. According to Clark & Porter (2004), there are at least two different generations of young stars within the G 305 radio complex. The first generation is associated with the massive clusters Danks 1 and 2, which contain many massive OB and Wolf-Rayet stars. The well known Wolf-Rayet star WR48a is projected

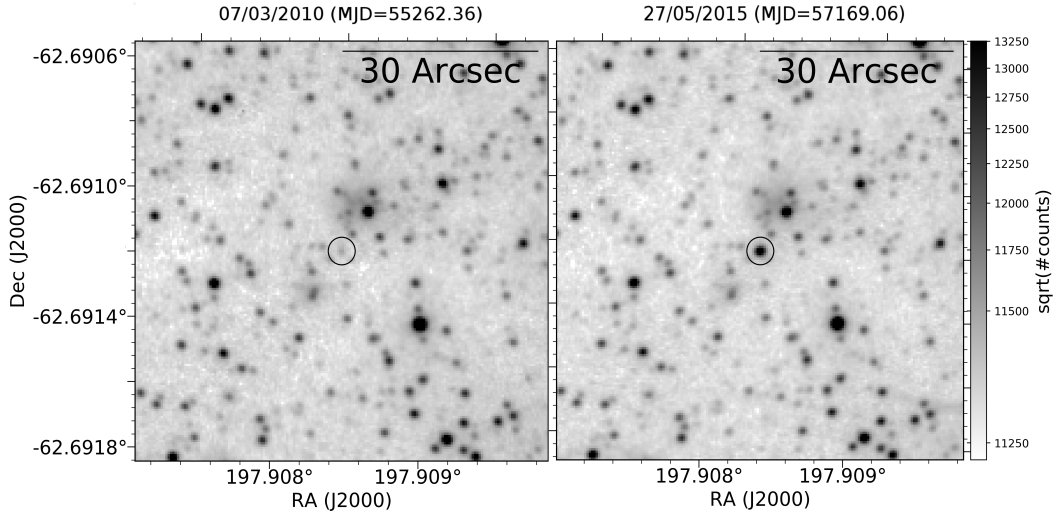


Figure 1. An example of a variable star, denominated d084.v8. Different epochs are indicated in the top of each image, the bar shows the square root of measured counts.

nearby. The presence of a dusty WCL star implies a minimum age of ~ 3 Myr and the lack of the red supergiants in the region suggests a maximum age of ~ 4 -5 Myr. The second generation consists of embedded IR sources, maser emission and ultracompact H II regions (UCHIIs; Hindson et al. 2012). A significant portion of the radio emission comes from the regions which coincide with the periphery of the mid-IR nebula (Clark & Porter 2004).

This is the second paper of our series on this region. In Borissova et al. (2019), we used moderately high resolution spectroscopy obtained with the Apache Point Observatory Galaxy Evolution Experiment-2 (APOGEE-2; Majewski et al. 2017) spectrograph to study the massive stellar content in the area. We investigated 29 OB type, Wolf-Rayet, and emission-line stars, adding 18 newly identified objects to the existing catalogs. Thus, we improved the census of the hot stellar population in the region. The average spectroscopic and Gaia DR2 distances are obtained as 3.2 ± 1.6 kpc and 3.7 ± 1.8 kpc, respectively. The OB stars have a mean radial velocity of $RV = -41.8 \text{ km s}^{-1}$. Eight objects show time-series variations in the K_S -bandpass with amplitudes greater than 0.5 mag. All of them, except 2MASS J13113560-6245324 (class 0/I YSO) and 2MASS J13160379-6242218 (OIf*/WN), are B type main sequence stars.

In this paper, we report a new study of the YSO population in the region. A variability search in the NIR K_S -bandpass is performed. Sources are identified as variable stars by their variability indices via analysis of the time-series data of the entire VVV survey period between 2010 and 2015. Spectroscopic follow-up of a sample is performed with the APOGEE-2 spectrograph. Finally, we collated catalogs of YSOs and candidate YSOs from the literature in order to investigate their spatial distribution.

2. VARIABILITY SEARCH

The VVV is an ESO NIR public survey (Minniti et al. 2010; Saito et al. 2012) which uses the 4-meter VISTA telescope (Sutherland et al. 2015) at Cerro Paranal Observatory, Chile. It was designed for mapping 562 deg^2 in the Galactic bulge and the southern disk in five NIR broad-band filters: Z , Y , J , H , and K_S , which has a time coverage spanning over five years, between 2010 and mid-2015. The observations were performed with the VIRCAM NIR camera (Dalton et al. 2006), which is an array of 16 detectors with 2048×2048 pixels each. The disk area is divided into 152 observing areas ($1.5 \times 1.2 \text{ deg}$ each, called tiles) and the bulge is covered with 196 tiles. Currently, the observed disk and bulge regions are extended by the ongoing VVX ESO public survey (Minniti 2018). The multi epoch observations are performed only in K_S . The VVV data were our main source of information for identifying stellar objects with variable brightness.

According to radio observations (Hindson et al. 2012), the projected diameter of the G 305 complex is 30 pc, at 3.5 kpc distance. Thus, the complete region is covered by four VVV tiles, namely d045, d046, d083 and d084, with total area of $\sim 7 \text{ deg}^2$. The selected regions and the total field of view (FoV) are shown in Figure 2.

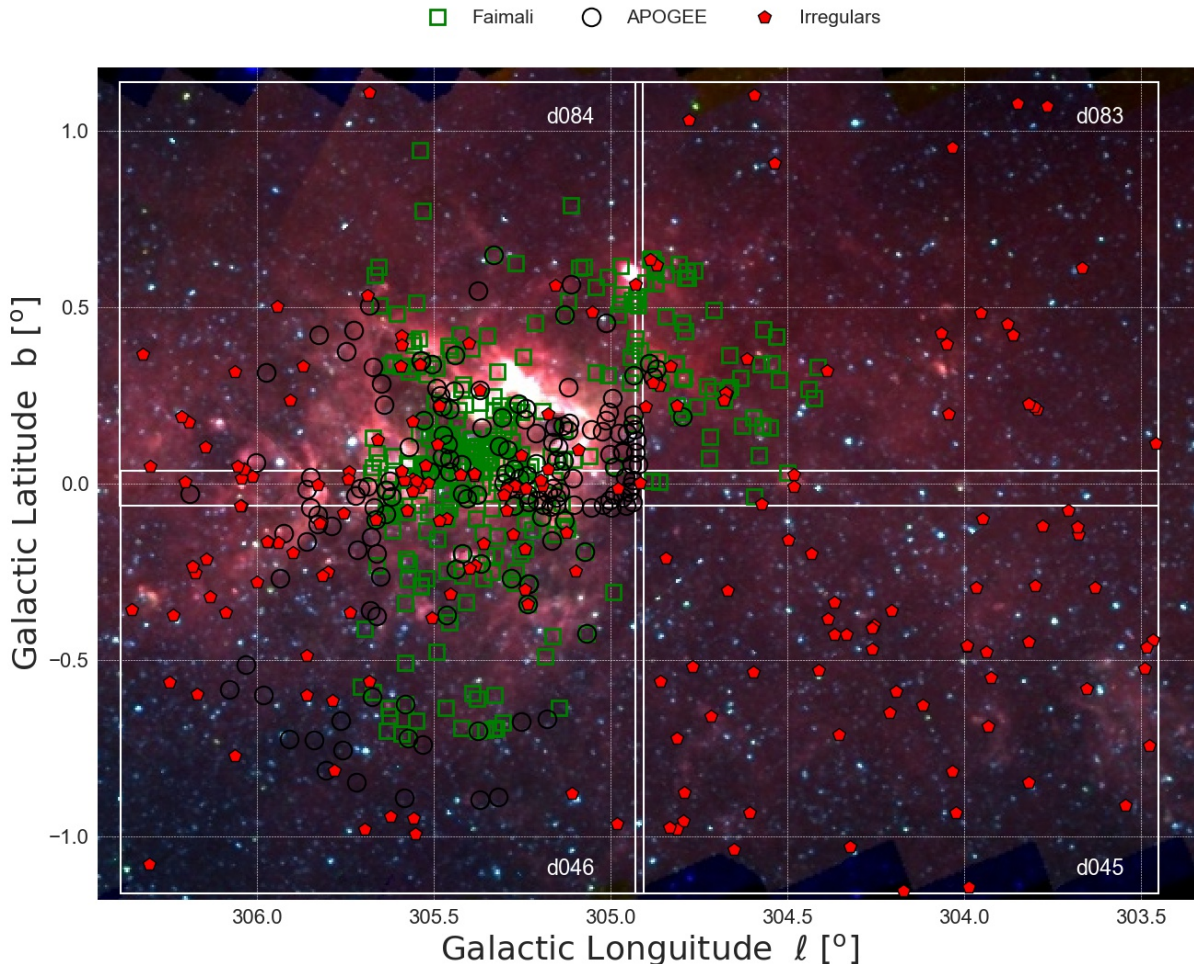


Figure 2. The G 305 star-forming complex region. The four observed tiles, named d045, d046, d083, and d084 from the VVV survey are labeled. The symbols represent different sets of YSOs and candidates discussed in this paper (see text). In the background, false three-color GLIMPSE Infrared Array Camera (IRAC; Fazio et al. 2004) image of the complete field is shown, using $8.0\mu\text{m}$ (red), $4.5\mu\text{m}$ (green), and $3.6\mu\text{m}$ (blue). Galactic north is up, galactic east is to the left.

In order to identify and characterize variable sources in the FoV, we used the automated tool presented in Medina et al. (2018). Briefly, each pawprint image was retrieved from the VISTA Science Archive¹ (VSA; Cross et al. 2012). Then, point spread function (PSF) photometry was obtained using the *Dophot* software (Schechter et al. 1993; Alonso-García et al. 2012) in all available images. The calibration process on to the VISTA system was done using the aperture photometry catalogs produced by the Cambridge Astronomical Survey Unit² (CASU, v1.3 pipeline). We selected sources with flags -1 (“Stellar”) or -2 (“Border-line stellar”) morphological classification to perform the cross-match, using a tolerance of $0.''34$ (the VISTA pixel size). The conversion factors and uncertainties were estimated using a linear fit to the *Dophot* PSF photometry vs. selected, well isolated CASU sources. A 2σ clipping was used in the linear model to avoid the scatter caused by fainter sources ($K_s \sim 16 - 17$ mag) in both photometric catalogues. We also included VVV tile images with flag “deprecated = 50”, which indicate the atmospheric seeing $> 2''$ during the observation. These images are found to be still useful for variability measurements, after careful inspection. In total, we generated and analyzed 3,570,064 K_s light curves of stars that populate the complete FoV. Table 1 lists some basic information of the tiles, such as identification number, coordinates, and the number of available epochs. The number of sources with time-series and the number of irregular variables are also reported.

¹ <http://horus.roe.ac.uk/vsa>

² <http://casu.ast.cam.ac.uk/>

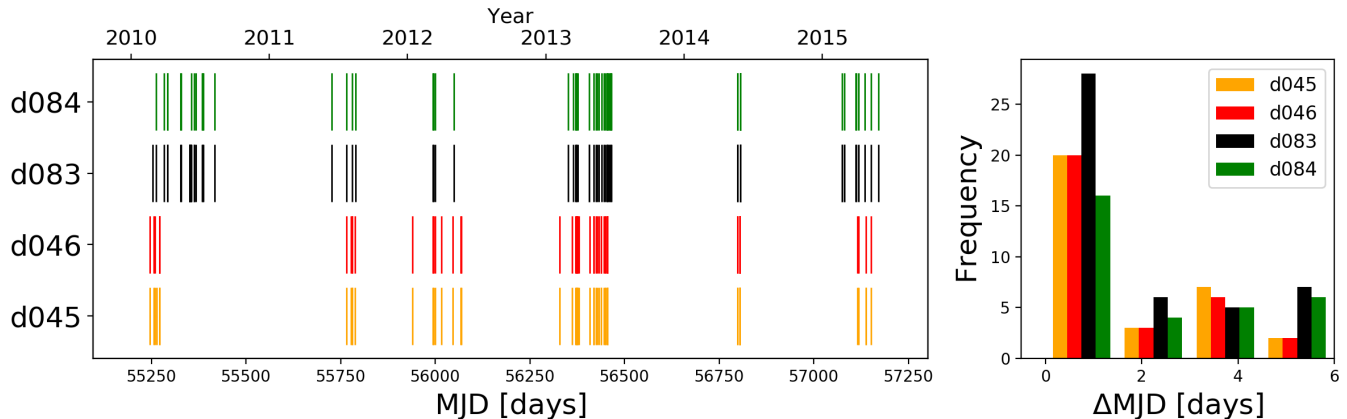


Figure 3. Left panel: Cadence of the selected VVV tiles. Each photometric measurement is represented by a ‘|’ symbol. The bars are thicker in places with high cadence. Right panel: Histogram of differences between consecutive observations ΔMJD . The color codes represent the same tiles in each plot.

As shown in Figure 3, VVV produces unevenly sampled time-series (Scargle 1982) that vary in sampling and cadence from tile to tile. As can be seen in the right panel, the typical time interval between observations is between 0.3 and 1.6 days for all tiles. Thus, the cadence of observations are well suited to detect short timescale variability in YSOs, related to short term accretion rate variations, episodic accretion events, rotational modulation by star spots and variable extinction (Rebull et al. 2014a). In fact, some studies have already been published regarding these topics and based on VVV data: Contreras Peña et al. (2017a,b) and Lucas et al. (2017) cataloged high amplitude eruptive variable stars; Borissova et al. (2016) searched for YSOs around young stellar clusters; Teixeira et al. (2018) measured variability in intermediate luminosity YSOs and massive YSO candidates; Medina et al. (2018) defined a new class of slowly varying YSOs, the so called “Low Amplitude Eruptive (LAE)” variables; and Guo et al. (2020) identified “multiple timescale variables” that are highly variable on timescales of weeks and years.

VVV tile ID	Central coordinates (ℓ [°], b [°])	Epochs	Sources with time-series	Irregular sources
d045	(304.2,-0.5)	55	950,085	57
d046	(305.7,-0.5)	54	1,068,806	66
d083	(304.2,0.5)	74	754,122	32
d084	(305.7,0.5)	59	797,051	41

Table 1. Summary of the VVV observations, sources with performed PSF photometry and selected irregular variables in each tile.

Following Medina et al. (2018) we used two main variability indices, ΔK_S and η , to select the variable star candidates. These two indices capture two fundamental properties of variable sources: the maximum change in brightness and the level of correlation among consecutive observations. The ranges of values of interest for each index were determined from their dispersion. The ΔK_S distribution was characterized using a non-parametric fit to determine the behavior of ΔK_S as a function of $\overline{K_S}$. Then the dispersion, σ , in ΔK_S as a function of $\overline{K_S}$ was measured. Sources with amplitude above 4σ were selected. For the η index, we assumed that the index comes from a Gaussian distribution and used, therefore, the σ parameter of the fitted distribution was used as a proxy for the standard deviation. Sources more than 3σ below the mean were considered for the method, given the fact that an η value that tends toward zero, is a strong indicator of variability (Sokolovsky et al. 2017). More specifically, in this study, we selected any star with $\Delta K_S > 0.6$ mag AND η values < 0.95 as a variable source.

Then, we searched for periodicity in the time series using the *Generalized Lomb-Scargle Periodogram* (GLS; Zechmeister & Kürster 2009) and the *Information Potential Metric* Q_m (IP metric; Huijse et al. 2011). We classified 177

variable stars as periodic (e.g. RRL, LPV). Their analysis will be the subject of a forthcoming paper and they are removed from the list of variable stars presented in this paper.

Under the above constraints we found 196 variable sources without any periodicity. Figure 4 shows the ΔK_S distribution for the sources found in the FoV, where red dots represent the selected *irregular variable sources*.

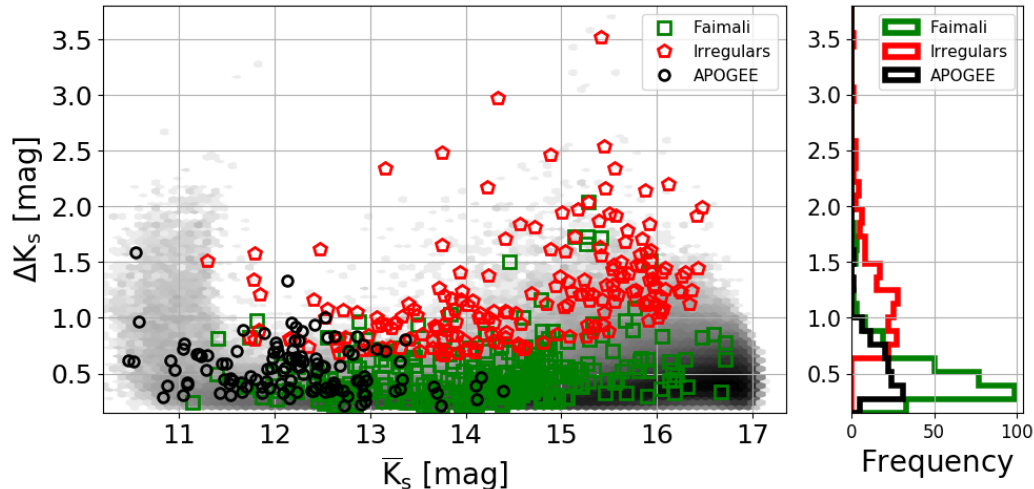


Figure 4. Left panel: Amplitude ΔK_S distribution as a function of the average K_S magnitude for different samples of YSOs considered in this paper. Right panel: Amplitude histogram for the different considered datasets. Colours and shapes are displayed in the top part of the plot. In the background, the amplitudes of all objects in tile d045 are shown for comparison.

Part of the complete sample of the irregular variable sources are listed in Table 5, and some examples of time-series are shown in Figure 5.

3. COMPARISON WITH PREVIOUSLY KNOWN YSOs IN G 305

YSOs in the G 305 region have been investigated by Faimali (2013), Robitaille et al. (2008), Contreras Peña et al. (2017a), and Marton et al. (2019). These data-sets were cross-matched with our time-series catalogs for d045, d046, d083 and d084 VVV tiles (using a tolerance of 0.4 arcsecs), in order to compare them with our catalog of irregular variable sources.

Faimali (2013): in this work the authors combined data from 2MASS, the first two years (2010-2011) of the VVV survey, the Spitzer Space Telescope (Werner et al. 2004) Galactic Legacy Infrared Midplane Survey Extraordinaire (GLIMPSE; Benjamin et al. 2003), Multiband Infrared Photometer for Spitzer aboard the Spitzer Space Telescope (MIPSGAL; Carey et al. 2009), MSX, and the Herschel infrared Galactic Plane Survey (Hi-GAL; Molinari et al. 2016) observations to conduct the first YSO census of G305. They detected 599 YSOs, but the published catalog reports only 339 of them. The authors estimated that their catalog is complete up to $\mathcal{M} > 2.6$ solar masses. From those, 319 have K_S time-series in our catalogs, but only six (IDs d046.v8, d046.v9, d046.v22, d083.v23, d084.v17 and d084.v24; see Table 5) are identified as irregular variable sources by our criteria.

Contreras Peña et al. (2017a): they reported 13 sources with an amplitude $\Delta K_S > 1$ mag, that were classified either as YSO candidates or long period variables (LPVs). We recovered 12 of them. Four stars are in common with the catalog reported here (V51, V482, V43 and V480 in their list). Three sources have a well defined period and are removed from our catalog: V816 ($P=616.9$ d), V45 ($P=584,6$ d), and V49 ($P=696.5$ d). Another four did not fulfill the η index criteria, having η index larger than the average selection value: V42 ($\eta = 1.4$), V44 ($\eta = 1.05$), V481 ($\eta = 1.25$), and v48 (with $\eta = 0.93$). Source V476 has $\eta = 0.6$, but an amplitude $\Delta K_S = 0.818$ mag, thereby passing the threshold in amplitude but not passing the threshold in η .

Robitaille et al. (2008): intrinsically red sources their catalog of extremely red objects contains sources classified as YSOs, YSOs candidates or Asymptotic Giant Branch (AGB) candidates. Those stars were selected from the

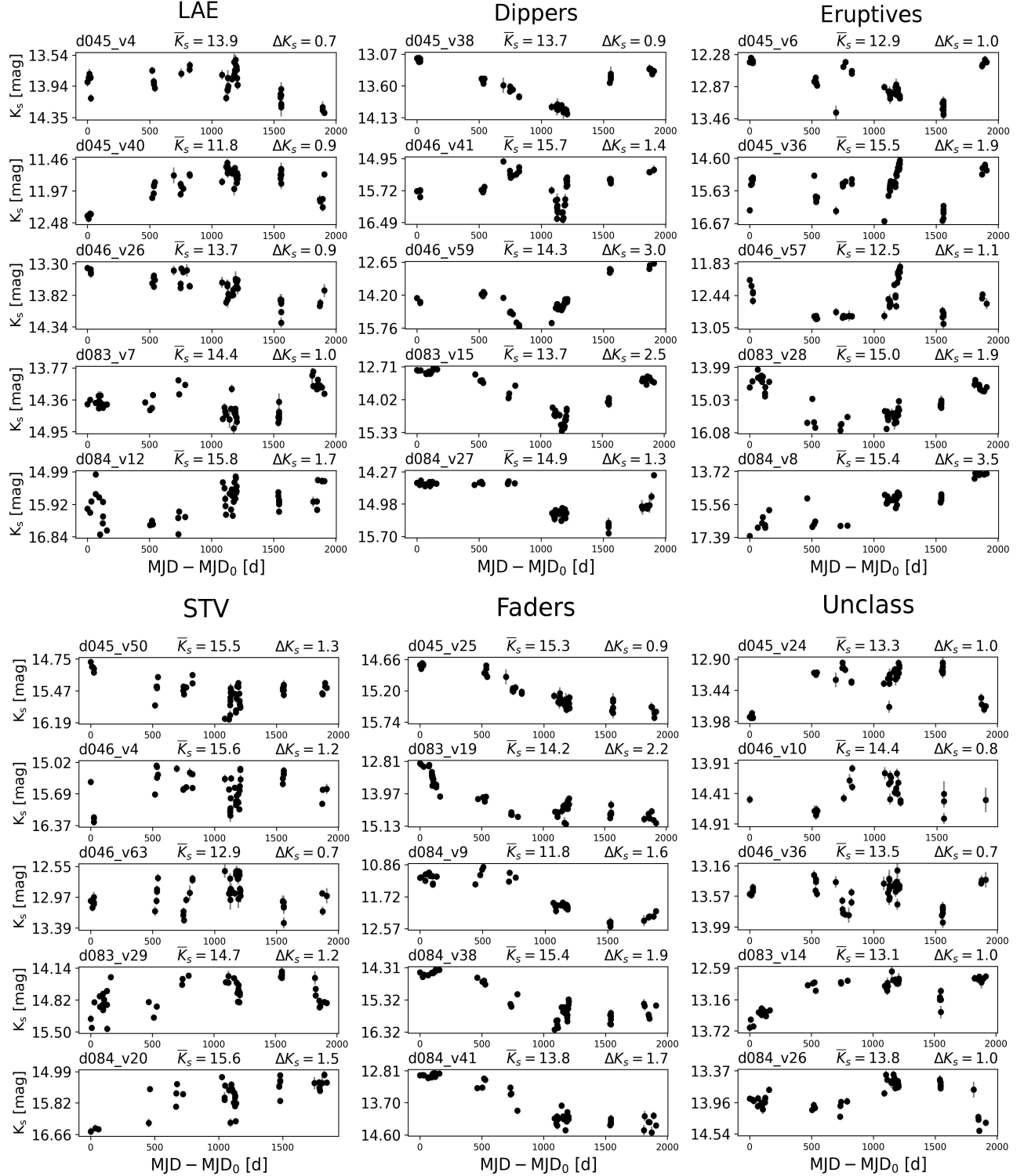


Figure 5. Examples of K_S -band time-series of irregular variables explained in section 4. Variable class for each plot group is indicated at the top. Also, for every time-series, the identification ID, mean magnitude \bar{K}_S and amplitude ΔK_S are shown. MJD_0 represent the modified julian date of the first detection for each time-series. The associated uncertainties is not visible given the amplitude of the variability.

GLIMPSE I and II surveys, based on their MIR color excess. There are 71 sources projected in our FoV, and nineteen of them have been identified also as irregular variable sources (see Table 5).

SIMBAD database (Wenger et al. 2000): we found 4 sources in common between this database and ours. The source d046_v12 (Borissova et al. 2016), named DBS130 Obj1, is a member of the cluster DBS[2003] 130. The source d046_v40 is identified in a maser catalog of Pestalozzi et al. (2005). The source d083_v29 is identified as an outflow candidate in Chen et al. (2011) and Cyganowski et al. (2008). Finally, the source d084_v41 is a well known nova called NOVA Cen 2005 or V1047 Cen (Samus 2005). It is interesting to note that the recently reported outburst in V1047 Cen (Aydi et al. 2019) is suggested to be a dwarf nova eruption.

Marton et al. (2019): finally, we cross-matched Faimali (2013), Robitaille et al. (2008), and our sample of irregular sources with the all-sky catalogue of YSO candidates of Marton et al. (2019). The authors combined the Gaia DR2 data with Wide-field Infrared Survey Explorer (WISE) and Planck measurements using machine learning techniques. We found only 65 stars in common, which is not surprising taking into account that our sources are much fainter than the optical Gaia DR2 data, as illustrated in Figure 6. From those, 44 stars (68%) are identified as YSOs, with $P_Y > 0.9$ probability. Thus, NIR studies are a useful addition to optical surveys.

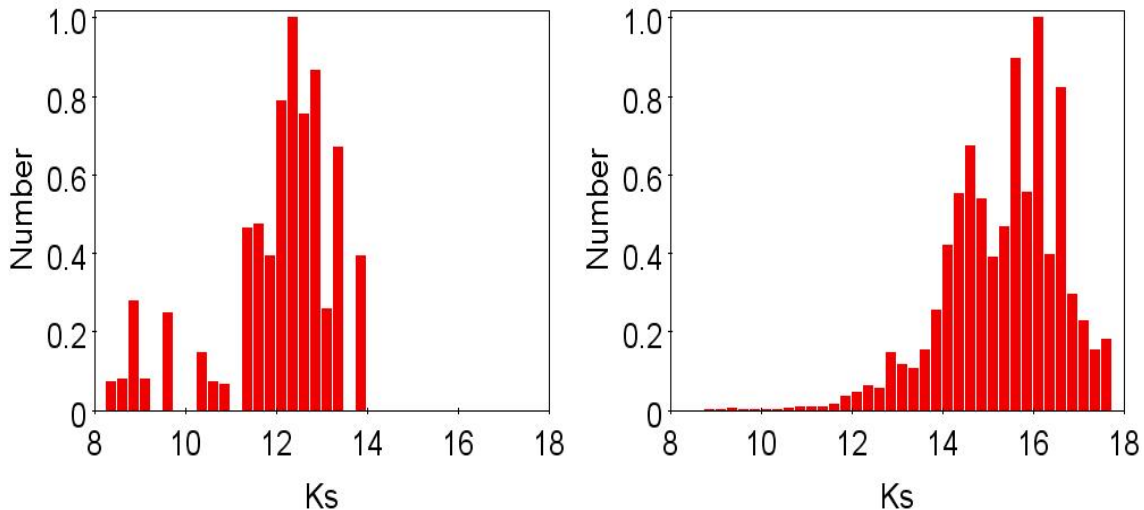


Figure 6. The histogram of K_S magnitudes of Marton et al. (2019) catalogue of YSO candidates (left) and the combined catalog of NIR YSOs. The magnitudes are taken from the VVV database.

The relatively small number of common objects is indicative of the very conservative and stringent selection criteria of our sample ($\Delta K_S > 0.6$ mag and η values < 0.95). Nevertheless, we decided to report only highly reliable variable sources, rather than a list containing all possible candidates. We are aware that we can have omitted a true irregular variable source and thus have reduced the completeness of the sample. However, by this approach we will have few false positive detections. Thus, the total number of newly proposed irregular variable sources is 167. Most probably, according to their light curves and irregularity, these objects are YSO candidates. Although recent studies (e.g. Cody et al. 2014; Contreras Peña et al. 2017a, Zhen et al., in preparation) found periodicity in some of the YSOs, in general the high amplitude variations do not show well-defined periods. But variability alone is not enough to confirm their status. For example, it is hard to distinguish between YSO and LPV irregular light curves. Further follow-up observations and analysis are necessary to clarify their classification. Thus, conservatively, hereafter we will continue to call these objects *irregular variable sources*.

4. ANALYSIS AND CLASSIFICATION OF THE IRREGULAR VARIABLE SAMPLE

Figure 4 shows the amplitude ΔK_S distribution of the sources as a function of the mean \bar{K}_S magnitude. In the background, as gray hexagons, the distribution of amplitudes of the whole tile d046 is shown for comparison. The

amplitude interval (red open pentagons) is between $0.661 < \Delta K_S < 3.521$ mag with an average value of $\overline{\Delta K_S} = 1.22$ mag. Since the effects of saturation in VVV are substantial in the distributions for sources brighter than $\overline{K_S} \sim 11.5$ mag and amplitudes ΔK_S larger than 0.65 magnitudes, these sources are carefully verified. To further investigate the nature of this amplitude distribution, we compare our sample of irregular variable sources with the one from Faimali (2013). Sources in this sample (green open squares) have SED classifications mainly as Class 0/I/II sources and amplitudes in the range $0.135 < \Delta K_S < 2.04$ mag, with $\overline{\Delta K_S} = 0.494$ mag. The amplitude distribution of APOGEE sources (black open circles) is similar, with $0.131 < \Delta K_S < 1.58$ mag and an average value of $\overline{\Delta K_S} = 0.54$ mag. The right panel of Figure 4 shows the histogram of the ΔK_S distribution where our irregular sources are almost separated from the other two data sets in terms of amplitude ΔK_S covering the higher amplitudes.

Carpenter et al. (2001), constructed a simple model of variations in brightness induced by cold spots, assuming a photospheric effective temperature $T_{\text{eff}} \sim 4000$ K for stars with age ~ 1 Myr and mass $\sim 1 M_\odot$. According to this model, if the spot coverage in the photosphere is assumed not to be larger than 30%, the amplitude caused by this mechanism can be $\Delta K_S \sim 0.3$ magnitudes. This mechanism could explain part of the amplitude distribution. On the other hand, high amplitude variability on timescales from months to decades in pre-main sequence objects is usually associated with episodic accretion events, attributed to disk instabilities typical of the early stages of young stellar objects (VoroByov 2009; VoroByov et al. 2019).

As we discuss in section 1, different processes can be responsible for luminosity variations in young stars. One of the main issues in this field of research is to determine what the origin of those brightness changes is. Usually, the variability is a result of the contribution of various physical mechanisms, depending on the circumstances and environments of each particular source. In some cases, this contribution can be dominated by one of these mechanisms and then it is possible to associate the morphology of the changes as a function of time with a certain type of variability.

Several authors have quantified the morphology of these time series to create a connection with certain processes, but this classification depends strongly on the type of data that we are analyzing. As an example, Rebull et al. (2014a), Wolk et al. (2015), and related papers within the YSOVAR project framework defined several types of variable stars using the MIR time-series from the Spitzer Space Telescope. The data sets from this telescope have different cadences and times for each SFR analyzed, where the periodic, quasi-periodic, and eruptive variable sources have been classified.

For the VVV survey, NIR irregular variable sources have been split in five categories related mainly to the time-scales of the variations and the *overall*, most common, state: Eruptive, Faders, Dippers, Short Time-scale Variable (STV) and Low Amplitude Eruptive (LAE). These categories are summarized in Table 2. The classification aims to highlight the main physical process that controls the variability. The scheme was used in Contreras Peña et al. (2017a), Medina et al. (2018), and references therein, in an effort to identify variable sources with VVV time-series. It is necessary to point out that, given the unevenly sampled time-series, some sources present more than one of the discussed features and will remain unclassified. Thus, for the 195 variables from our list (excluding NOVA Cen 2005, source d084_v41, see above) we find 47 irregular variable sources with eruptive characteristics, 25 dippers, 17 faders, 24 LAE, 37 short-term variables, and 45 sources remain unclassified. Examples of these categories are shown in Figure 5 and the classification assigned is listed in the final table of irregular variables (Table 5). However, it is necessary to mention that some stars may have alternative classifications: d045_v4 and d046_v26 could be faders; d083_v7 could be a dipper; d084_v12 could be an STV, because short term scatter has highest amplitude; and d045_v24 and d083_v14 could be eruptive variables. Thus, we added the CCD analysis to the light curve morphological classification, and some spectroscopic follow-up is planned to better reveal their true category.

5. ($J - H$) VS. ($H - K_S$) COLOR-COLOR DIAGRAM

Additionally to the K_S photometry described above, we also obtained the J - and H -bandpass photometry. Again, we used the *Dophot* software to perform PSF photometry in the first epoch (2010) of our VVV observations. The transformation to the standard system was performed using a linear fit between the aperture photometry from CASU and the PSF photometry. The total photometric uncertainty for each measurement is proportional to each individual PSF measurement deviation, and the standard deviation σ_{clip} obtained from the linear fit. The final uncertainties were computed as $\sigma_{\text{phot}} = \sqrt{\sigma_{\text{PSF}}^2 + \sigma_{\text{clip}}^2}$, giving ~ 0.25 mag at $J \sim 19$ -19.5 mag, and ~ 0.18 mag at $H \sim 18.5$ -19 mag. Due to the VVV observational strategy, both J - and H data were taken in the same night with differences ranging from only a few minutes to not more than a few hours. The standard deviation of the linear fits and the MJD for each observation are listed in Table 3. In the areas of overlap between different tiles, when both measurements were available, the average value was adopted. There are 18 sources that have been identified in two different tiles: 16 in

Class	Description	N° of sources
Dippers	Shows one or more fading events on a timescale of months or years, followed by a return to normal brightness.	25
Eruptives	Shows sources with outbursts with amplitude > 1 mag and duration longer than a few days and typically at least a year.	47
Low Amplitude Eruptive	Sources that present outbursts with amplitude lower than 1 mag and duration typically longer than a year.	24
Short Timescale Variables	Sources where the time series is dominated by fast variability on timescales from days to weeks. They also can show brief bursts in brightness on timescales of weeks.	37
Faders	The light curve is best described by a monotonic decrease in brightness on a timescale $t > 1$ yr, sometimes following a constant brightness initially	17
Unclassified	Sources without a clear trend.	45

Table 2. Characterization of aperiodic VVV K_S light curves of YSOs proposed by Contreras Peña et al. (2017a) and extended by Medina et al. (2018)

tiles d046 and d084, one in d045-d083 and one in d083-d084. Sources having J and H magnitudes that were averaged across two tiles are marked in the final catalog. It should be noted that the sources do not have large discrepancies between their magnitudes in the J and H bands. They are in the order of 0.2 mag in H , and 0.1 mag in J attributable to a combination of variability and measurement uncertainties.

Tile ID	K_S MJD	J, H MJD	σ_{clip} J mag	σ_{clip} H mag	Cross-matched sources
d045	55264	55263	0.062	0.101	1,094,833
d046	55271	55271	0.047	0.048	1,182,601
d083	55254	55253	0.105	0.062	682,920
d084	55262	55261	0.04	0.07	837,668

Table 3. The MJD, the standard deviation from PSF calibration σ_{rmclip} and the cross-matched sources for all considered tiles in G 305.

As pointed out by Hindson et al. (2012), the G 305 region contains dust clumps spread over the field, which produce extinction towards the stellar sources. A widely used technique to characterize such highly reddened sources is their position in the CCD. Particularly, as disused in Lada & Adams (1992) on the NIR ($J-H$, $H-K_S$) plane, the stars with intrinsic excess emission, heavily reddened sources, and stars with normal photospheric colors can be distinguished from each other. For further analysis, we use ($J-H$, $H-K_S$) CCDs for the 2010 epoch. To create the CCD we used the closest K_S epoch in time to the J and H images. For the tiles d045, d083 and d084 the images were observed with one day of separation, meanwhile for d046 K_S data were taken on the same night as the J and H photometry. To perform the cross-match between catalogs, we used a tolerance of 0.4 arcseconds in all the selected regions. Table 3 contains the MJD for each image and the quantity of cross-matched sources for each VVV tile. Then, we divide the ($J-H$, $H-K_S$) plane following the method of Sugitani et al. (2002) and Ojha et al. (2004). The sources are analyzed with respect to the loci followed by main-sequence stars, giant stars, and classical T-Tauri stars defined in Bessell & Brett (1988) and Meyer et al. (1997). Three regions can be distinguished as follows:

1. F-region: We define the region between the reddening vectors of main-sequence stars and giant stars as the F-region. These objects are considered to have at most a small NIR excess, likely corresponding to Class III or Class II YSOs. Some of these could be foreground or background sources.
2. T-region: The T-region is defined to be between the projected reddening vector from the end of the T-Tauri locus (Meyer et al. 1997) and the main-sequence dwarf reddening vector. Sources located here are considered to

have a substantial NIR excess and are likely to be Class II objects, also known as T-Tauri stars. Some Herbig Ae/Be sources with small NIR excess are also considered to lie in the T-region.

3. P-region: The region to the right of the reddening vector extending from the end of the T-Tauri locus is called the P-region. The projected sources in this region are more likely Class I objects, sources with thermal emission from the circumstellar envelope, and protostar-like and/or Herbig Ae/Be objects.

In general, only a subset of all objects has been detected in J and H bands, but still 130, 179 and 127 of our irregular variables, the [Faimali \(2013\)](#) sample, and the APOGEE sample, respectively, have reliable JH measurements and can be placed in the CCD (see Fig. 7). Sources have been displayed in a CCD for each selected VVV tile, where the entire population of each tile is plotted in the background. Solid black lines correspond to unreddened main-sequence stars and giant stars sequence ([Bessell & Brett 1988](#)). Solid red line represents the intrinsic T-Tauri locus ([Meyer et al. 1997](#)). The reddening vectors using the [Rieke & Lebofsky \(1985\)](#) extinction law and assuming a visual extinction $A_V = 15$ mag for each evolutionary track are also shown.

In total, we were able to classify 116 of our irregular variable sources.

Only a small fraction of them falls inside the F-region between the reddening vectors projected from the intrinsic color of main-sequence stars and giants. The majority are near to the red border of this region and probably are Class III/Class II sources with small NIR excess. The rest of the sample falls redward of the F-region, thus indicating the presence of intrinsic infrared excess emission, a distinctive feature of young sources with circumstellar matter.

T-region sources are located redward of the F-region, but blueward of the reddening line projected from the red end of the T Tauri locus. They are considered to be mostly classical T-Tauri stars (Class II objects) with clear NIR excess. This is consistent with the type of stellar objects that we expect to identify given their IR variable nature. To support this interpretation, we built the membership histogram for all selected sources (top histogram in figure 7). About 60% of identified irregular sources are located inside the T-region.

Protostellar sources (i.e., Class I YSOs) are expected to lie redward of the reddening vector of the classical T Tauri (CTT) locus, in the so-called P-region, given they are intrinsically red due to their evolutionary state. Some $\sim 20\%$ of the whole sample falls in this region.

A substantial part of the [Faimali \(2013\)](#) YSO sample ($\sim 63\%$) lies in the T-region. The right panel of Figure 7 shows the membership histogram of each category.

Most stars from the APOGEE sample fall in the F-region. Also, in the CCD they populate areas characterized by low values of visual extinction, close to unreddened loci of main sequence stars and giants.

The above membership assignments of the sources will only be considered as a preliminary estimate of their evolutionary stage.

6. MIR PHOTOMETRY AND SED CLASS

In order to better analyze the irregular variables, we cross-identified our sample with the GLIMPSE IRAC catalog. IRAC provides the highest spatial resolution of any mid-IR imager for panoramic surveys over wavelengths from 3 to 9 μm . The IRAC photometry is much more reliable near the Galactic plane than the WISE photometry, which was severely limited there by detector saturation and especially by source confusion. We also made a cross-identification with 24 μm Spitzer/MIPS band, which unfortunately is not available for the vast majority of the point sources detected in GLIMPSE. For this reason, we made an additional cross-match with the WISE catalog, from which we used only W4 photometry.

In order to assess the evolutionary stages of YSOs in our sample, we used the infrared spectral index, α . The value of the index depends on the spectral range. The wider the range towards the MIR, the higher the sensitivity to different kinds of disks. Additionally, the calculation of the spectral index is also affected by the reddening ([Indebetouw et al. 2005](#)). To estimate values that are minimally affected by the reddening, we use the wavelength range from 4.5 μm to 24 μm . The interstellar extinction in these bands is smaller than at shorter wavelengths, and the reddening curve is flatter. We obtained α following the procedure and using the equations given in [Kuhn et al. \(2020\)](#):

$$\alpha_{[4.5]-[24]} \approx 0.55([4.5] - [24]) - 2.94,$$

$$\alpha_{[4.5]-W4} \approx 0.58([4.5] - W4) - 2.92,$$

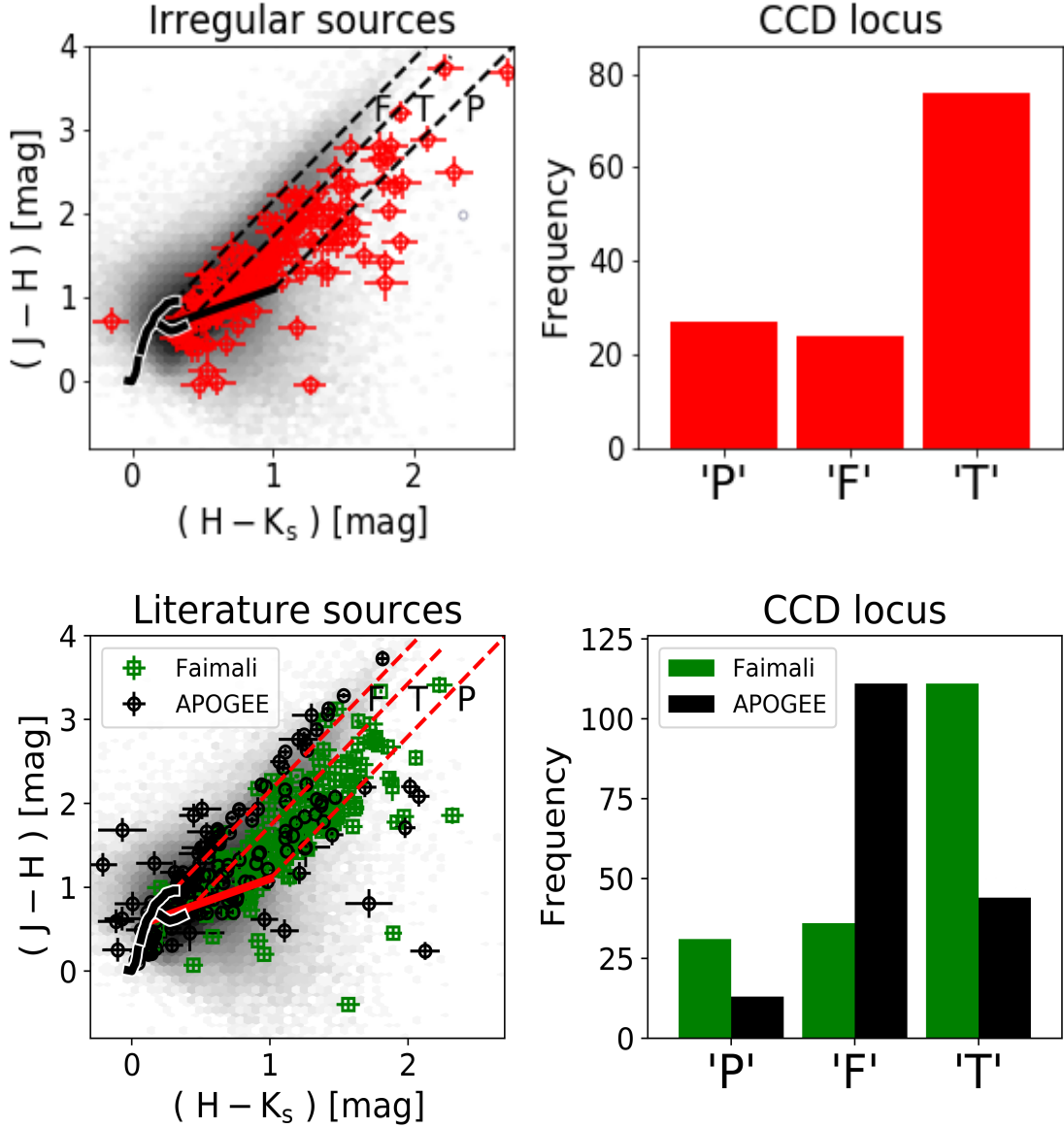


Figure 7. Left panels: CCDs for all selected tiles in VVV, displaying the so-called F, T and P-regions. In the background of the CCDs, as blue hexagons, the color distribution of tile d046 is shown as a comparison. Right panels: The histograms with the CCD classification.

$$\alpha_{[4.5]-[8.0]} \approx 1.64([4.5] - [8]) - 2.82.$$

All data from GLIMPSE, MIPS and WISE are given in Table 5.

As in Kuhn et al. (2020), we prefer the α estimate based on $[4.5] - [24]$, followed by $[4.5] - W4$, and finally $[4.5] - [8.0]$. The morphology of the $([4.5] - [5.8])$ vs. $[5.8] - [8.0]$ CCD shows that in our sample, there are no YSOs presenting strong silicate absorption or PAH emission.

From the entire list of 196 variables, there are IRAC, MIPS, and/or WISE data for 116 objects ($\sim 59\%$ of all), allowing us to obtain the index α for all of them. The α values and the corresponding Class are given in Table 5.

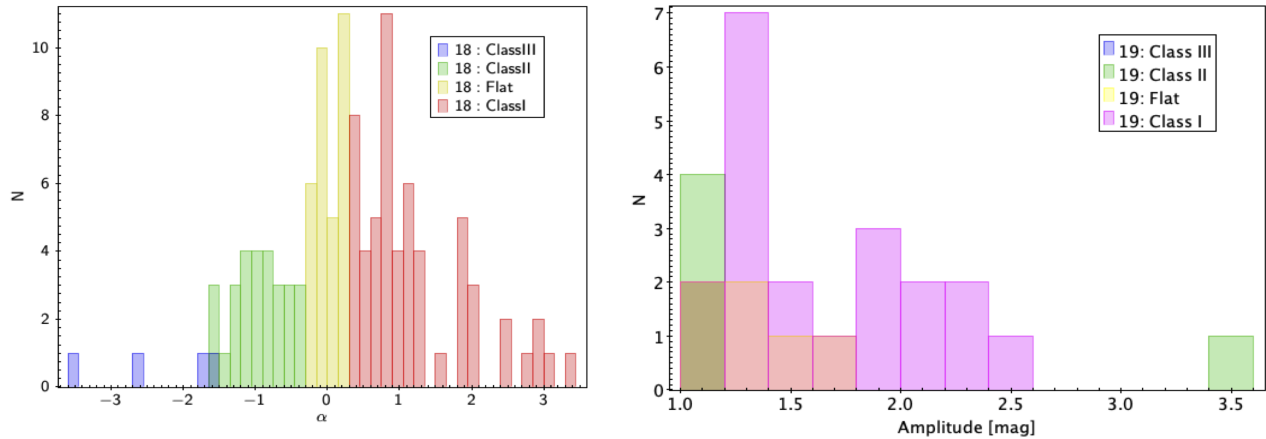


Figure 8. Left panel. Histogram distribution of spectral indices for 116 YSOs with MIR photometry, subdivided into YSO class using the customary demarcations at $\alpha = -1.6, -0.3$, and 0.3 . Right panel. Histogram distribution of the amplitudes of the objects classified as *Eruptive*.

Figure 8 (Left panel) shows the distribution of the spectral indices for YSOs. Subdivision into YSO classes is made using the limits at $\alpha = -1.6, -0.3$, and 0.3 (Greene et al. 1994). Based on these criteria, there are 58 Class I ($\alpha > 0.3$), 32 Flat spectrum ($0.3 \geq \alpha > -0.3$), 28 Class II ($-0.3 \geq \alpha > -1.6$), and only 4 Class III ($\alpha \geq -1.6$) YSOs.

The shape of the distribution depends on the relative number of the YSO classes. In general, Class II/III YSOs should be more common than Class I/Flat SED YSOs due to the longer lifetimes of the later evolutionary stages (Evans et al. 2009). But our study, based on variability, is initially limited by the amplitude ($\Delta K_S \geq 0.6$), which is expected to exclude higher proportions of Class III and Class II YSOs than Class I YSOs. This is clearly visible in Figure 8 (Left Panel). So, we are much more sensitive to the younger YSO population.

Additionally, we analyze the amplitude distribution for the YSOs classified as *Eruptive*, shown in Figure 8 (Right panel). Not surprisingly, Class III objects are missing in this figure. The Class II YSOs show lower amplitudes of about 1 mag. The Flat spectrum objects are concentrated between 1 and 1.6 mag, and the Class I, as expected, span the whole range from 1 to 2.5 mag. The only exception in this classification is d084-v8, which is classified as Class II, but shows the highest amplitude of 3.52 mag. Most probably, it is a result of a wrong α index, obtained only by the WISE W4 magnitude and missing [8.0] and [24] measurements. Also, the NIR classification for this object is missing, because it is too faint and too red, and has no J and H measurements.

7. APOGEE-2 SAMPLE

APOGEE-2 (Majewski et al. 2017) is a second generation multi-object NIR spectrograph (Wilson et al. 2019), mounted on the 2.5 meter du Pont Telescope at Las Campanas Observatory, Chile (Gunn et al. 2006). It is the successor to APOGEE and it is part of the Sloan Digital Sky Survey IV (Blanton et al. 2017). The observed spectral range is 1.51-1.70 μm , with resolution $R=22500$. Approximately 300 stars can be observed per plate, typically assigning about 250 fibers for science targets, 35 for sky, and 15 for telluric stars, with the fiber collision limit of about $70''$. To design the strategy for spectroscopic follow-up, we assigned priorities for observation based on the preliminary classification of the objects: 59% are stars with infrared variability in K_S band from our search (priority 1); 21% (priority 2) are from the Faimali (2013) catalog; 8% (priority 3) are extremely red sources from Robitaille et al. (2008); 3% show X-ray emission (Chandra Source Catalog Evans et al. 2010); 7% are probable members of the clusters VVV CL 021, CL 022, CL 023 and CL 024 (Borissova et al. 2011), and three stars (2%) are classified as high proper motion candidates (Kurtev et al. 2017). The last three groups were added as “fillers”, during the target selection process. The APOGEE-2 observations of G 305 were carried out on April 14, 2017 (under external CNTAC program No. CN2016B90), with 1 hour exposure time. The data were processed by the APOGEE Stellar Parameter and Chemical

Abundances Pipeline (Nidever et al. 2015; García Pérez et al. 2016), which includes basic data reduction, combination of spectra from multiple visits, and measurement of radial velocities, stellar parameters and elemental abundances.³

In total, 127 stars were observed with APOGEE-2. Their spectra are analyzed using the TONALLI (L. Adame, in prep.) spectral classification code. In brief, the TONALLI code is based on the *Asexual Genetic Algorithm* (Cantó et al. 2009) to find the closest match among a synthetic model grid using a multi-dimensional approach based on a set of parameters. The code uses the Phoenix (Allard et al. 2013) atmosphere model grid with "solar" abundances between $-0.1 < M/H < 0.6$ and $-0.1 < \alpha/Fe < 0.1$, after pre-selecting "low temperature" star candidates with $T_{\text{eff}} < 8000$ K. As a result of the best fit, it derives the abundances $[Z]$, $[\alpha/Fe]$, $\log g$, $v \sin i$, and radial velocities (RV).

In the case of G 305, 122 stars are classified by the tool as YSOs, but 25% of them have S/N between 2 and 10 and lower weight (between 0.2 and 0.5) was assigned for their parameters during the analysis. Figure 9 shows the distribution of their fundamental parameters. The measured effective temperature T_{eff} peak is around 4000K, in agreement with Carpenter et al. (2001). There is a peak in $[\alpha/Fe]$ around 0.2 but the mean value of $[\alpha/Fe]=0.02\pm 0.13$. The Z/Z_{\odot} distribution has a peak around -0.2 , but a second peak around 0.5 can be also identified. The mean Z/Z_{\odot} of 0.11 ± 0.27 reveals that the YSOs in G 305 are slightly super-solar in metal abundance. The radial velocity peak is around -41 km/s.

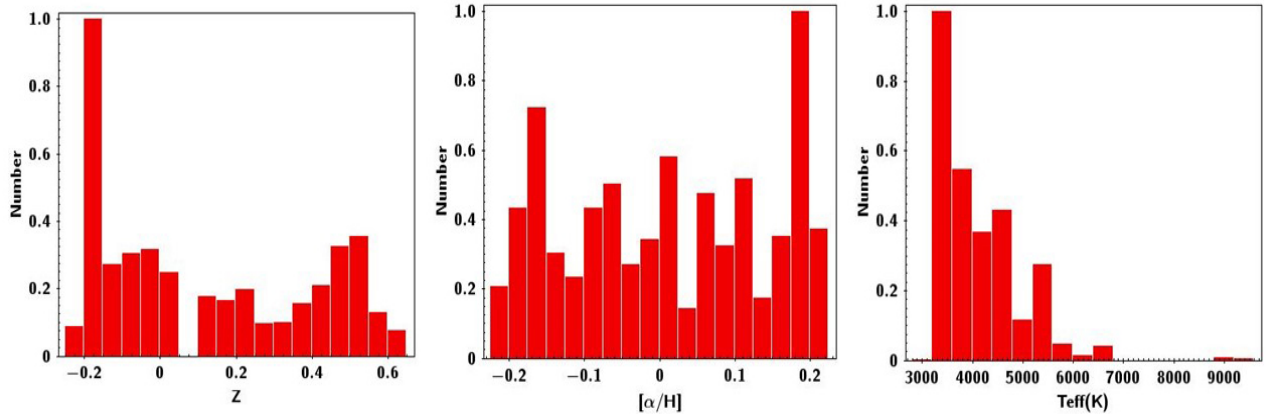


Figure 9. Distribution of YSOs according to their fundamental parameters derived with APOGEE-2: Histograms of metallicity (Z/Z_{\odot}), α elements, and T_{eff} . All parameters are measured by the TONALLI tool.

A cross match with the Gaia DR2 proper motion, parallax, and distance (Bailer-Jones et al. 2018) catalogs found 104 stars in common. The average distance is calculated as 3.7 ± 0.7 kpc. Comparison with radial velocities and distance of the OB stars in the region (Borissova et al. 2019) shows no significant differences from a kinematic point of view between the two stellar populations.

With regard to the variability of these YSOs, Figure 4 shows the distribution of their amplitudes. As can be seen, in general, they have smaller amplitudes compared to the irregular variable sources from our list (marked with red symbols). Nevertheless, all of them have amplitudes between $0.209 < \Delta K_S < 1.587$ mag – an average of 0.54 mag –, thus showing some kind of variability. We could not find any correlation between fundamental parameters and the amplitude of variability. We calculated the Pearson correlation coefficients of $[M/H]$ vs. Amplitude to be ≈ -0.4 ; $[Fe/H]$ vs. Amplitude to be ≈ -0.4 ; $[\alpha/H]$ vs. Amplitude to be ≈ -0.4 ; T_{eff} vs. Amplitude to be ≈ -0.4 ; and $\log g$ vs. Amplitude to be ≈ -0.4 . Taking into account the relatively small number of stars, we found these correlation coefficients to be statistically insignificant.

As has been pointed out, three stars (VVVJ 13081183-6317548; VVVJ 13081329-6242491 and 2M13182865-6253076) classified as high proper motion objects (Kurtev et al. 2017) were observed by APOGEE as "fillers". Although far from the main topic of the paper, we analyzed them and will briefly mention here. The Gaia DR2 data shows that they can be measured in the optical waveband too and indeed they have large proper motions (Table 4). Comparing the

³ For more details see <http://www.sdss.org/dr14/algorithms/>

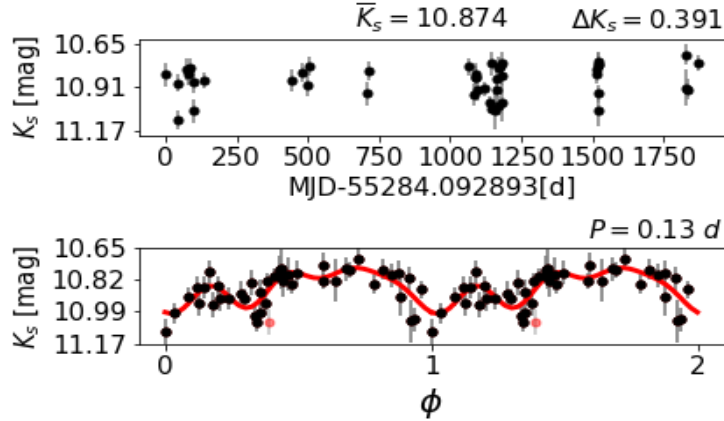


Figure 10. Time-series (top panel) and folded light curve with a $P=0.13$ [days] (low panel) of source 2M13121845-6237309. The period has been found using the IP metric (Huijse et al. 2011). The red line in the folded light curve represents the harmonic fit, and red points are the rejected measurements of the 3σ clipping of the fit.

Gaia temperature vs. the [Straizys & Kuriliene \(1981\)](#) spectral type and the Spectroscopic type vs. $\log g$ (measured by APOGEE spectra) calibrations, we derived their spectral types. Although this classification has an uncertainty of 2-3 subtypes, these are identified as K and early M-type stars rather than ultracool dwarfs. From the X-ray emitters, only 2M13121845-6237309 has a tentative period of 0.13 days and its light curve resembles that of a binary star (Figure 10).

8. SPATIAL DISTRIBUTION AROUND THE G 305 SFR

The location of the identified irregular variable sources can be seen on the panoramic view of the G 305 star-forming complex shown in Figure 2. The main data sets considered in this study are marked with different symbols and colors. The false-color view provided by the Spitzer Space Telescope InfraRed Array Camera (IRAC) at mid-infrared wavelengths of $3.6\mu\text{m}$ to $8\mu\text{m}$ is in the background. As can be seen, the selected irregular sources extend throughout the whole area. However, the density distribution is different: the sources in tiles d046 and d084 are mostly projected on the red filaments across the image. These trace the polycyclic aromatic hydrocarbons (PAH) emission, excited by surrounding interstellar radiation and become luminescent at wavelengths near $8.0\mu\text{m}$. The PAH emission is typically found from photo-dissociated regions (e.g. [Hollenbach & Tielens 1997](#)). On the other hand, the sources in the tiles d045 and d083 show a nearly homogeneous distribution. Thus, the distribution of the young sources in G 305 clearly trace the ongoing star-formation zones. Some individual examples are shown in Figure 11, where the sources d045_v18 and d045_v35 are projected in the IRAC bands on green nebulosity, indicating an outburst or jet that is bright at $4.5\mu\text{m}$. The right panels show the d084_v6 and d084_v20 sources projected on nebulous regions in 2MASS images.

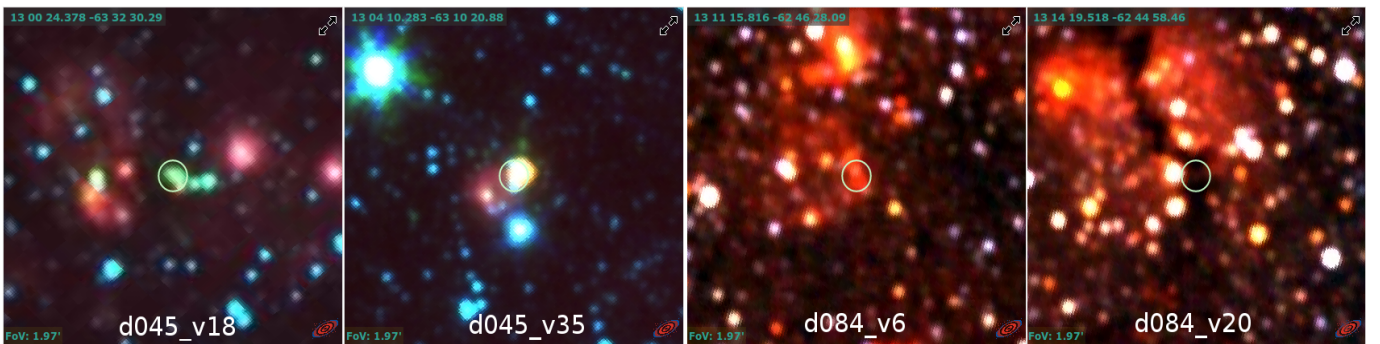


Figure 11. Examples of sources projected in a different environment overlapped on IRAC (two on the left) and 2MASS (two on the right) bands false color images.

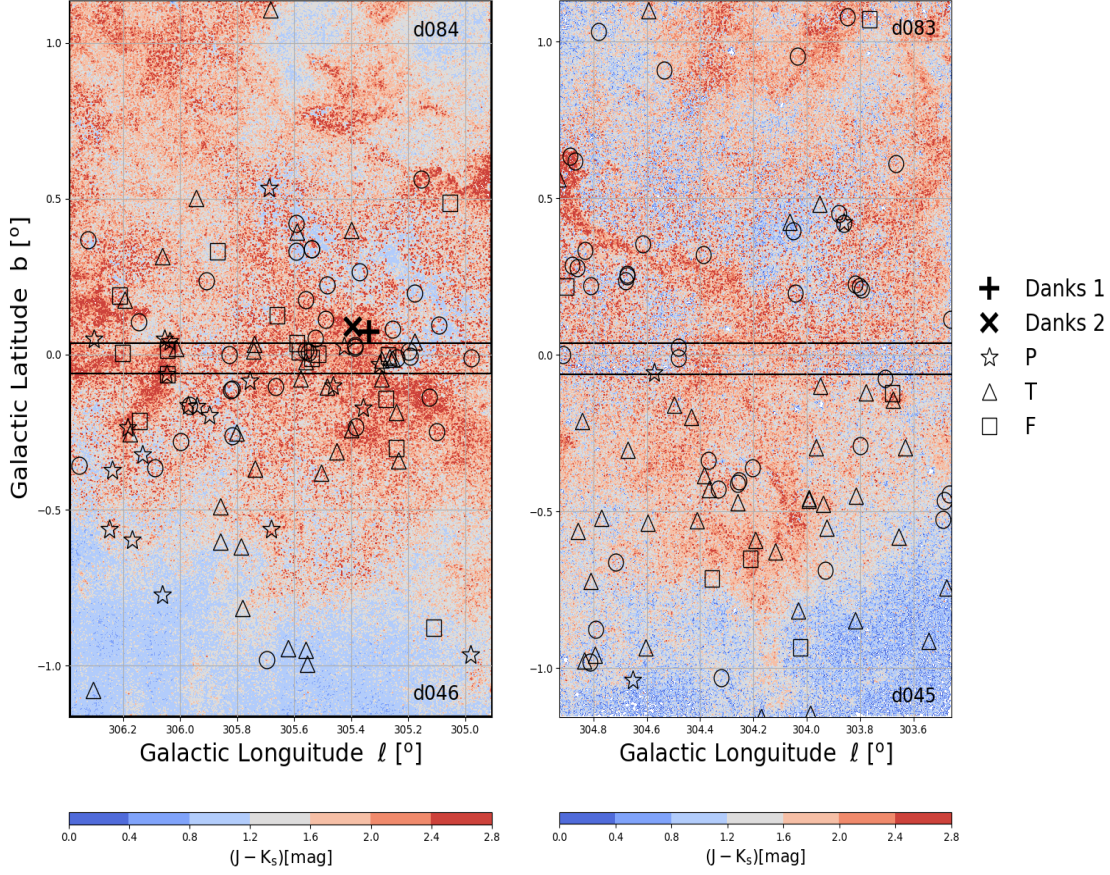


Figure 12. Distribution of the observed $J - K_S$ colors of the stars in G 305 region with variable irregular sources overplotted. Open circles, represent the sources without color. The horizontal lines mark the overlapping zone of the tiles d084-d046, and d083-d045 respectively. The symbols for the P, T and F-objects, as well as for the position of the clusters Dansk 1 and 2, are given on the right.

The spatial projection of the classified variables can be also illustrated with the smoothed surface ($J - K_S$) color distribution shown in Figure 12. Considering that class I/II objects (comparing with class III) are more likely to show variability due to their instability while evolving towards the main-sequence (Rice et al. 2015; Contreras Peña et al. 2017a) one should expect that they are distributed and concentrated in dust and gas over-densities. This trend is clearly visible in G 305 region.

As mentioned before, in this paper we analyzed several catalogs, which contain YSOs or YSO candidates: Faimali (2013), Contreras Peña et al. (2017a), Robitaille et al. (2008), the APOGEE-2 confirmed YSOs, and the irregular variable sources derived from the VVV K_S band analysis, comprising a total of 700 stars. We will consider this catalog as a statistically representative sample of YSOs and candidates in the region. The sample was cross-identified with Gaia DR2, yielding 295 stars with proper motion measurements. As can be seen in Figure 13, their distribution is typical for a structure belonging to the galactic disk. The stars form a compact group centered on $\mu_\alpha \cos \delta \approx -7.5 \text{ mas yr}^{-1}$ and $\mu_\delta \approx -0.5 \text{ mas yr}^{-1}$.

Moreover, the distribution projected on the sky is not random, but in fact most of the sources are concentrated within the central cavity formed by two massive clusters, namely Danks 1 and 2 (Faimali 2013; see also Figure 2, where different catalogs are color-coded). The mean surface density of the YSOs in the region is calculated to be 0.025 YSOs/pc⁻², while the central cavity contains 10 times more objects per area (0.238 YSOs/pc⁻²), clearly tracing the propagation of star formation in the region.

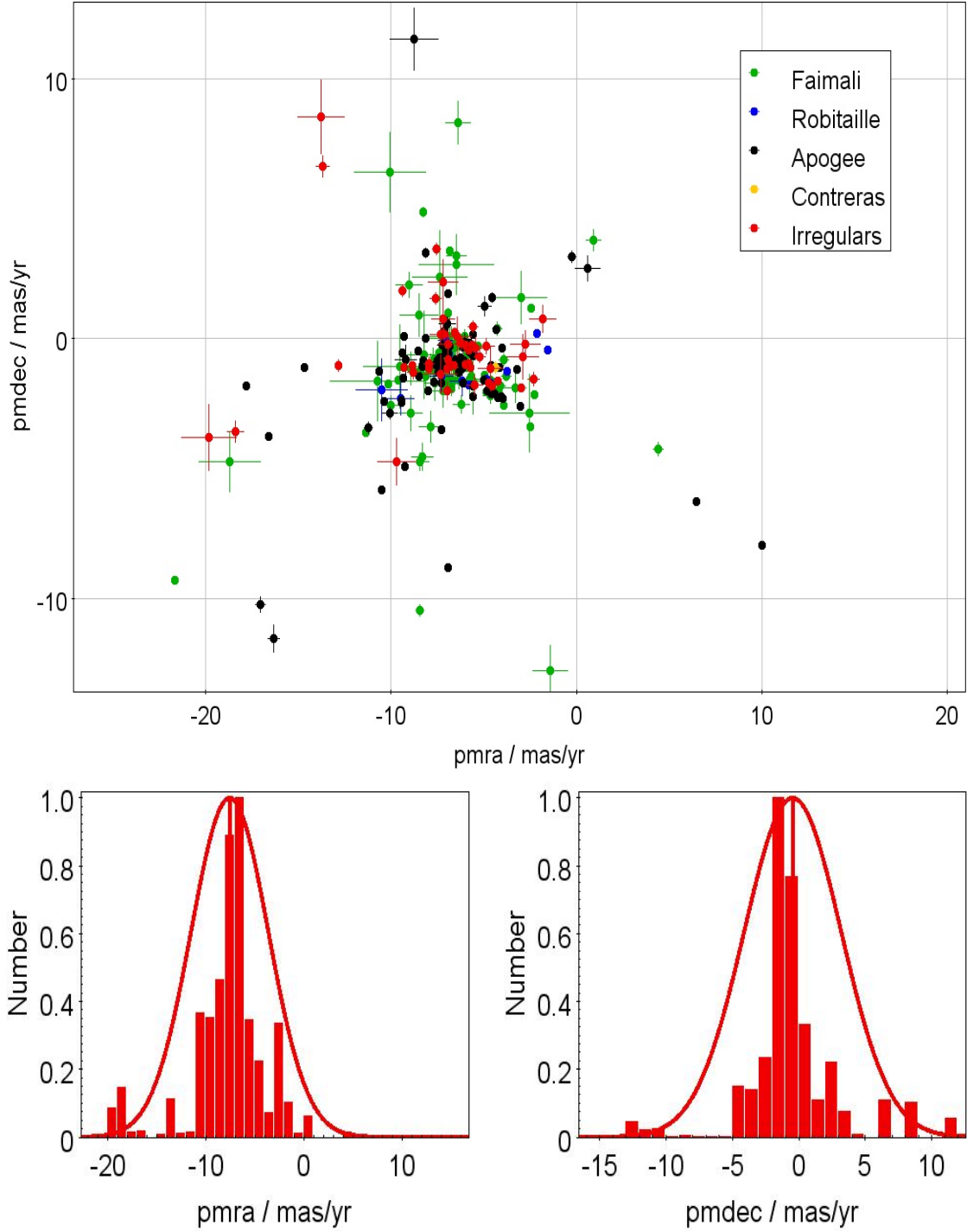


Figure 13. Up: The kinematic distribution of YSOs with measured proper motions from Gaia DR2. The different data sets are shown in colors, explained in the legend (see text). Down: The histograms of $\mu_{\alpha} \cos \delta$ and μ_{δ} with Gaussian function overplotted.

9. DISCUSSION AND SUMMARY.

G 305 is a relatively close-by, luminous giant HII region with active star formation. Using the time-series photometry in the K_S bandpass provided by the VVV survey for the sources in this region, we generated and analyzed 3,570,064

unevenly sampled light curves over a 5-year period. The variability indices $\Delta K_S > 0.6$ mag and η values < 0.95 are used in order to select variable star candidates. We found 373 high-amplitude variable candidates in the region: 177 sources show periodicity in their variability, while 196 seem to show irregular variations in their brightness. After cross correlation with catalogs of YSOs available in the literature and SIMBAD, 167 stars are identified as new irregular variable stars. Inspection of the light curves indicates that these objects are good YSO candidates. On the basis of the morphology of their light curves, the sources are classified using Medina et al. (2018) scheme: Eruptive, Faders, Dippers, STVs, and LAEs. It is interesting to mention, that from classified variables the biggest group (31%) contains Eruptive sources, confirming that the eruption is a frequently physical mechanisms for the brightness changes.

Additionally, the YSOs from the different catalogues from the literature Robitaille et al. (2008); Faimali (2013); Contreras Peña et al. (2017b) are analyzed. The $(J - H)$ vs. $(H - K_S)$ CCDs are constructed and the position of variable sources on the diagrams are connected with their evolutionary status (Class I, Class I/II and Class III). About 60% of the identified irregular sources are located at the so-called T-region. This region encompasses variables with large NIR excess, and is usually regarded as the probable location of Class II systems. In order to improve this classification, we cross-identified our sample of 196 non-periodic variables with GLIMPSE, MIPS, and WISE catalogs. There are available data for 116 of them. Using the infrared α index, we classified these 116 objects as follows: 58 Class I, 32 flat spectrum, 28 Class II, and only 4 Class III YSOs. Thus, the majority of highly variable YSOs with mid-IR detections are classified as Class I systems, even if they are located in the T- region of the near IR two colour diagram. (Sources lacking mid-IR detections are of course more likely to be Class II or Class III systems). The high proportion of Class I YSOs clearly reflects the ongoing star formation in G 305 region. Comparing with the OB stellar population, we can support the Clark & Porter (2004) suggestion of sequential star formation.

In total, 127 stars were observed with the APOGEE-2 multi-object NIR spectrograph. From them, 122 stars are classified by the TONALLI code as YSOs. The mean Z/Z_\odot of 0.11 ± 0.27 suggests that the YSOs in G 305 are slightly super-solar in metal abundance. The radial velocity peak is around -41 km/s. The average distance of 3.7 ± 0.7 kpc is calculated, on the base of Gaia DR2 distance catalog. Thus, we do not find any significant differences from a kinematic point of view between the YSOs and OB stellar population (Borissova et al. 2019) in the region. All stars with APOGEE-2 spectra are variable, with amplitudes between $0.209 < \Delta K_S < 1.587$ mag in the K_S band.

The spatial distributions of the combined catalog of 700 YSOs in G 305 shows that the distribution is not random, but in fact the YSOs are concentrated within the central cavity formed by the massive clusters Danks 1 and 2. We find the mean surface density of YSOs to be 0.025 YSOs/pc $^{-2}$, while the central cavity contains 10 times more objects per area (0.238 YSOs/pc $^{-2}$).

10. ACKNOWLEDGMENTS

We thank the referee for carefully reviewing the manuscript and for the valuable suggestions and comments. We gratefully acknowledge data from the ESO Public Survey program ID 179.B-2002 taken with the VISTA telescope, and products from the Cambridge Astronomical Survey Unit (CASU), also on data products from observations made with ESO Telescopes at the La Silla, Paranal Observatory under program ID 177.D-3023, as part of the VST Photometric H_α Survey of the Southern Galactic Plane and Bulge (VPHAS+). This work was funded by ANID – Millennium Science Initiative Program – ICN12.009 awarded to the Millennium Institute of Astrophysics (MAS). N.M. acknowledges support through a Fellowship for National PhD students from ANID, grant number 21181952. J.A.-G. acknowledges support from Fondecyt Regular 1201490. A.B. acknowledges funding by ANID, Millennium Science Initiative, via the Núcleo Milenio de Formación Planetaria (NPF) and from FONDECYT Regular 1190748. A. Roman-Lopes acknowledges financial support provided in Chile by Comisión Nacional de Investigación Científica y Tecnológica (CONICYT) through the FONDECYT project 1170476 and by the QUIMAL project 130001. C. Román-Zúñiga acknowledges support from project CONACYT CB2018 A1-S-9754 and project UNAM-PAPIIT IN112620, Mexico.

Funding for the Sloan Digital Sky Survey IV has been provided by the Alfred P. Sloan Foundation, the U.S. Department of Energy Office of Science, and the Participating Institutions. SDSS-IV acknowledges support and resources from the Center for High-Performance Computing at the University of Utah. The SDSS web site is www.sdss.org.

SDSS-IV is managed by the Astrophysical Research Consortium for the Participating Institutions of the SDSS Collaboration including the Brazilian Participation Group, the Carnegie Institution for Science, Carnegie Mellon University, the Chilean Participation Group, the French Participation Group, Harvard-Smithsonian Center for Astrophysics, Instituto de Astrofísica de Canarias, The Johns Hopkins University, Kavli Institute for the Physics and Mathematics of the Universe (IPMU) / University of Tokyo, the Korean Participation Group, Lawrence Berkeley

National Laboratory, Leibniz Institut für Astrophysik Potsdam (AIP), Max-Planck-Institut für Astronomie (MPIA Heidelberg), Max-Planck-Institut für Astrophysik (MPA Garching), Max-Planck-Institut für Extraterrestrische Physik (MPE), National Astronomical Observatories of China, New Mexico State University, New York University, University of Notre Dame, Observatório Nacional / MCTI, The Ohio State University, Pennsylvania State University, Shanghai Astronomical Observatory, United Kingdom Participation Group, Universidad Nacional Autónoma de México, University of Arizona, University of Colorado Boulder, University of Oxford, University of Portsmouth, University of Utah, University of Virginia, University of Washington, University of Wisconsin, Vanderbilt University, and Yale University.

Software: `Matplotlib` (Hunter 2007), `NumPy` (Oliphant 2006), `AstroPy` (The Astropy Collaboration et al. 2018), `Sklearn` (Pedregosa et al. 2011), `AstroML` (Vanderplas et al. 2012), `Dophot` (Schechter et al. 1993; Alonso-García et al. 2012), `VOSA` (Bayo et al. 2008), `STILTS` (Taylor 2006).

Name	$\alpha(2000)$	$\delta(2000)$	$[\alpha/H]$	$\log g$	T_{eff}	RV	π (mas)	$\mu_{\alpha} \cos \delta$	μ_{δ}	G	BP-BR	Sp type	
VVVJ13081183-6317548	197.0492770	-63.2985550	0.4501	-0.0997	4.8207	4340	-70.32	3.9893±0.1396	-69.497±0.163	-1.755±0.165	13.91	1.59	K5-7
VVVJ13081329-6242491	197.0553602	-62.71362753	0.0518	-0.0437	5.1028	3846	9.24	15.0873±0.0305	-106.512±0.039	-115.861±0.039	13.42	2.40	M3-5
2M13182865-6253076	199.6193776	-62.88544519	0.5706	-0.0994	5.1461	4951	-17.55	5.3724±0.2526	-80.335±0.346	-26.341±0.36	12.74	1.285	K3-5

Table 4. High proper motion stars observed by APOGEE.

01D [3-6]	$\alpha(2000)$ [4-5]	$\delta(2000)$ [4-5]	l [4-5]	b [5-8]	Mean K_S [5-8]	K_S err [8-0]	Nobs [8-0]	Ampl [24]	η [24]	TileID	K_S 55264 mag_err4	W1	W1err	W2	W2err	J	J err	H	H err	$H - H - K_S$	Class	Var	Class	Comment	Reference	
d045-v1	194.045408	-63.311269	303.4645635	-0.4444275	16.422	0.032	42	1.444	0.414	d045																
14.051	0.099	13.213	0.095	12.326	0.143	11.541	0.063	7.87	0.1											0.459	Class I	LAE				
d045-v2	194.082928	-63.608539	303.4757633	-0.7419591	12.348	0.017	51	0.742	0.157	d045	11.889	0.058	13.659	0.121	12.616	0.098	1.043	0.727	T	Dipper						
11.176	0.075	10.888	0.073	10.551	0.089	10.378	0.074	5.51	0.07	10.766	0.03	10.49	0.027	8.738	0.184	4.854	0.104	0.176	Flat							
d045-v3	194.089278	-63.331243	303.4838829	-0.4647675	16.027	0.022	52	1.08	0.285	d045	15.663	0.059	17.522	0.067	1.859					Fader	in-group					
12.548	0.075	11.149	0.057	10.346	0.148																					
d045-v4	194.101456	-63.39115	303.4881923	-0.5247683	13.912	0.014	45	0.686	0.553	d045	13.807	0.058	17.063	0.066	3.256					LAE						Robitaille
9.91	0.038	8.612	0.038	7.376	0.024	6.773	0.022			10.161	0.023	8.255	0.019	5.98	0.025	3.652	0.024	-0.043	Flat							
d045-v5	194.242266	-63.77788	303.542943	-0.9126947	14.142	0.019	50	1.038	0.319	d045	13.576	0.058	15.01	0.12	14.154	0.098	0.856	0.578	T	Fader						
13.226	0.079	12.787	0.071	12.723	0.249	12.315	0.121													Class II						
d045-v6	194.406342	-63.158305	303.6303178	-0.2949481	12.858	0.023	51	1.049	0.458	d045	12.432	0.057	14.098	0.12	13.134	0.098	0.964	0.702	T	Eruptive	FIRE					
12.9	0.036	12.707	0.061	12.274	0.104	12.225	0.203			11.75	0.031	11.379	0.027	9.723	0.061	8.084	-0.239	Flat								
d045-v7	194.475246	-63.443083	303.654274	-0.5804006	14.287	0.015	53	0.8	0.447	d045	14.044	0.058	15.276	0.12	14.57	0.098	0.706	0.526	T	Dipper						
13.293	0.064	12.937	0.121	12.996	0.329	12.562	0.301													Class III						
d045-v8	194.502338	-63.006601	303.6775207	-0.1443672	13.714	0.026	46	1.265	0.609	d045	13.252	0.057	15.783	0.12	14.295	0.098	1.488	1.043	T	Eruptive						
11.906	0.042	11.203	0.034	10.564	0.044	9.666	0.022													Class I						
d045-v9	194.502973	-62.98427	303.6785789	-0.1220508	14.545	0.013	46	0.766	1.053	d045	14.204	0.057	15.593	0.12	14.643	0.098	0.95	0.439	F	STV						
13.457	0.046	12.9	0.065	12.349	0.107	11.514	0.05													Class I						
d045-v10	194.558735	-62.93687	303.7049504	-0.0753248	16.052	0.027	47	1.405	0.698	d045										STV						Robitaille
11.691	0.042	10.617	0.053	9.583	0.028	8.717	0.026			12.576	0.039	10.578	0.022	8.08	0.026	5.595	0.04	-0.007	Flat							

... And 186 more objects ...

Table 5. Parameters of the VVV variables considered in this work. Description of each column and the full version of the table is available at the CDS.

REFERENCES

- Allard, F., Homeier, D., Freytag, B., et al. 2013, *Memorie della Societa Astronomica Italiana Supplementi*, 24, 128
- Alonso-García, J., Mateo, M., Sen, B., et al. 2012, *AJ*, 143, 70
- Arnaboldi, M., Neeser, M. J., Parker, L. C., et al. 2007, *The Messenger*, 127, 28
- Audard, M., Abraham, P., Dunham, M. M., et al. 2014, in *Protostars and Planets VI*, ed. H. Beuther, R. S. Klessen, C. P. Dullemond, & T. Henning, 387
- Aydi, E., Strader, J., Chomiuk, L., et al. 2019, *The Astronomer's Telegram*, 12975, 1
- Bailer-Jones, C. A. L., Rybizki, J., Fouesneau, M., Mantelet, G., & Andrae, R. 2018, *AJ*, 156, 58
- Bayo, A., Rodrigo, C., Barrado Y Navascués, D., et al. 2008, *A&A*, 492, 277
- Benjamin, R. A., Churchwell, E., Babler, B. L., et al. 2003, *PASP*, 115, 953
- Bessell, M. S., & Brett, J. M. 1988, *PASP*, 100, 1134
- Blanton, M. R., Bershad, M. A., Abolfathi, B., et al. 2017, *AJ*, 154, 28
- Borissova, J., Bonatto, C., Kurtev, R., et al. 2011, *A&A*, 532, A131
- Borissova, J., Ramírez Alegría, S., Alonso, J., et al. 2016, *AJ*, 152, 74
- Borissova, J., Roman-Lopes, A., Covey, K., et al. 2019, *AJ*, 158, 46
- Cantó, J., Curiel, S., & Martínez-Gómez, E. 2009, *A&A*, 501, 1259
- Caratti o Garatti, A., Stecklum, B., Garcia Lopez, R., et al. 2017, *Nature Physics*, 13, 276
- Carey, S. J., Noriega-Crespo, A., Mizuno, D. R., et al. 2009, *PASP*, 121, 76
- Carpenter, J. M., Hillenbrand, L. A., & Skrutskie, M. F. 2001, *The Astronomical Journal*, 121, 3160.
<https://doi.org/10.1086%2F321086>
- Chen, X., Ellingsen, S. P., Shen, Z.-Q., Titmarsh, A., & Gan, C.-G. 2011, *ApJS*, 196, 9
- Clark, J. S., & Porter, J. M. 2004, *A&A*, 427, 839
- Cody, A. M., Stauffer, J., Baglin, A., et al. 2014, *AJ*, 147, 82
- Conti, P. S., & Crowther, P. A. 2004, *MNRAS*, 355, 899
- Contreras Peña, C., Lucas, P. W., Minniti, D., et al. 2017a, *MNRAS*, 465, 3011
- Contreras Peña, C., Lucas, P. W., Kurtev, R., et al. 2017b, *MNRAS*, 465
- Cross, N. J. G., Collins, R. S., Mann, R. G., et al. 2012, *A&A*, 548, A119
- Cyganowski, C. J., Whitney, B. A., Holden, E., et al. 2008, *AJ*, 136, 2391
- Dalton, G. B., Caldwell, M., Ward, A. K., et al. 2006, in *Proc. SPIE*, Vol. 6269, Society of Photo-Optical Instrumentation Engineers (SPIE) Conference Series, 62690X
- Davies, B., Hoare, M. G., Lumsden, S. L., et al. 2011, *MNRAS*, 416, 972
- Drake, A. J., Djorgovski, S. G., Mahabal, A., et al. 2009, in *American Astronomical Society Meeting Abstracts*, Vol. 213, American Astronomical Society Meeting Abstracts #213, 470.07
- Evans, Neal J., I., Dunham, M. M., Jørgensen, J. K., et al. 2009, *ApJS*, 181, 321
- Evans, I. N., Primini, F. A., Glotfelty, K. J., et al. 2010, *ApJS*, 189, 37
- Faimali, A. D. 2013, PhD thesis, University of Hertfordshire
- Fazio, G. G., Hora, J. L., Allen, L. E., et al. 2004, *ApJS*, 154, 10
- Frost, A. J., Oudmaijer, R. D., de Wit, W. J., & Lumsden, S. L. 2021, arXiv e-prints, arXiv:2102.05087
- Gaia Collaboration, Eyer, L., Rimoldini, L., et al. 2019, *A&A*, 623, A110
- García Pérez, A. E., Allende Prieto, C., Holtzman, J. A., et al. 2016, *AJ*, 151, 144
- Greene, T. P., Wilking, B. A., Andre, P., Young, E. T., & Lada, C. J. 1994, *ApJ*, 434, 614
- Gunn, J. E., Siegmund, W. A., Mannery, E. J., et al. 2006, *AJ*, 131, 2332
- Guo, Z., Lucas, P. W., Contreras Peña, C., et al. 2020, *MNRAS*, 492, 294
- Herbig, G. H. 1952, *JRASC*, 46, 222
- . 1966, *Vistas in Astronomy*, 8, 109
- Herbig, G. H. 1989, in *European Southern Observatory Conference and Workshop Proceedings*, Vol. 33, European Southern Observatory Conference and Workshop Proceedings, ed. B. Reipurth, 233–246
- Hindson, L., Thompson, M. A., Urquhart, J. S., et al. 2012, *MNRAS*, 421, 3418
- Hollenbach, D. J., & Tielens, A. G. G. M. 1997, *ARA&A*, 35, 179
- Huijse, P., Estevez, P. A., Zegers, P., Principe, J. C., & Protopapas, P. 2011, *IEEE Signal Processing Letters*, 18, 371
- Hunter, J. D. 2007, *Computing In Science & Engineering*, 9, 90
- Indebetouw, R., Mathis, J. S., Babler, B. L., et al. 2005, *ApJ*, 619, 931
- Ivezić, Ž., Kahn, S. M., Tyson, J. A., et al. 2019, *ApJ*, 873, 111
- Joy, A. H. 1945, *ApJ*, 102, 168

- Kaiser, N., Aussel, H., Burke, B. E., et al. 2002, Society of Photo-Optical Instrumentation Engineers (SPIE) Conference Series, Vol. 4836, Pan-STARRS: A Large Synoptic Survey Telescope Array, ed. J. A. Tyson & S. Wolff, 154–164
- Kuhn, M. A., de Souza, R. S., Krone-Martins, A., et al. 2020, arXiv e-prints, arXiv:2011.12961
- Kurtev, R., Gromadzki, M., Beamín, J. C., et al. 2017, MNRAS, 464, 1247
- Lada, C. J., & Adams, F. C. 1992, ApJ, 393, 278
- Li, Z. Y., Banerjee, R., Pudritz, R. E., et al. 2014, in Protostars and Planets VI, ed. H. Beuther, R. S. Klessen, C. P. Dullemond, & T. Henning, 173
- Lucas, P. W., Smith, L. C., Contreras Peña, C., et al. 2017, MNRAS, 472, 2990
- Majewski, S. R., Schiavon, R. P., Frinchaboy, P. M., et al. 2017, AJ, 154, 94
- Marton, G., Abraham, P., Szegedi-Elek, E., et al. 2019, MNRAS, 487, 2522
- McKee, C. F., & Ostriker, E. C. 2007, ARA&A, 45, 565
- Medina, N., Borissova, J., Bayo, A., et al. 2018, ApJ, 864, 11
- Meyer, M. R., Calvet, N., & Hillenbrand, L. A. 1997, AJ, 114, 288
- Minniti, D. 2018, in The Vatican Observatory, Castel Gandolfo: 80th Anniversary Celebration, ed. G. Gionti & J.-B. Kikwaya Eluo, Vol. 51, 63
- Minniti, D., Lucas, P. W., Emerson, J. P., et al. 2010, NewA, 15, 433
- Molinari, S., Schisano, E., Elia, D., et al. 2016, A&A, 591, A149
- Mottram, J. C., Hoare, M. G., Davies, B., et al. 2011, ApJL, 730, L33
- Nidever, D. L., Holtzman, J. A., Allende Prieto, C., et al. 2015, AJ, 150, 173
- Ojha, D. K., Tamura, M., Nakajima, Y., et al. 2004, ApJ, 616, 1042
- Oliphant, T. 2006, Guide to NumPy (MIT), 1–371. <https://web.mit.edu/dvp/Public/numpybook.pdf>
- Pedregosa, F., Varoquaux, G., Gramfort, A., et al. 2011, Journal of Machine Learning Research, 12, 2825
- Pestalozzi, M. R., Minier, V., & Booth, R. S. 2005, A&A, 432, 737
- Rebull, L. M., Cody, A. M., Covey, K. R., et al. 2014a, AJ, 148, 92
- . 2014b, AJ, 148, 92
- Rice, T. S., Reipurth, B., Wolk, S. J., Vaz, L. P., & Cross, N. J. G. 2015, AJ, 150, 132
- Rice, T. S., Wolk, S. J., & Aspin, C. 2012, ApJ, 755, 65
- Rieke, G. H., & Lebofsky, M. J. 1985, ApJ, 288, 618
- Robitaille, T. P., Meade, M. R., Babler, B. L., et al. 2008, AJ, 136, 2413
- Saito, R. K., Hempel, M., Minniti, D., et al. 2012, A&A, 537, A107
- Samus, N. N. 2005, IAUC, 8596, 2
- Scargle, J. D. 1982, ApJ, 263, 835
- Schechter, P. L., Mateo, M., & Saha, A. 1993, PASP, 105, 1342
- Sokolovsky, K. V., Gavras, P., Karampelas, A., et al. 2017, MNRAS, 464, 274
- Straizys, V., & Kuriliene, G. 1981, Ap&SS, 80, 353
- Sugitani, K., Tamura, M., Nakajima, Y., et al. 2002, ApJL, 565, L25
- Sutherland, W., Emerson, J., Dalton, G., et al. 2015, A&A, 575, A25
- Taylor, M. B. 2006, in Astronomical Society of the Pacific Conference Series, Vol. 351, Astronomical Data Analysis Software and Systems XV, ed. C. Gabriel, C. Arviset, D. Ponz, & S. Enrique, 666
- Teixeira, G. D. C., Kumar, M. S. N., Smith, L., et al. 2018, A&A, 619, A41
- The Astropy Collaboration, Price-Whelan, A. M., Sipőcz, B. M., et al. 2018, ArXiv e-prints, arXiv:1801.02634
- Vanderplas, J., Connolly, A., Ivezić, Ž., & Gray, A. 2012, in Conference on Intelligent Data Understanding (CIDU), 47–54
- Vorobyov, E. I. 2009, ApJ, 704, 715
- Vorobyov, E. I., Skliarevskii, A. M., Elbakyan, V. G., et al. 2019, A&A, 627, A154
- Wenger, M., Ochsenbein, F., Egret, D., et al. 2000, A&AS, 143, 9
- Werner, M. W., Roellig, T. L., Low, F. J., et al. 2004, ApJS, 154, 1
- Wilson, J. C., Hearty, F. R., Skrutskie, M. F., et al. 2019, PASP, 131, 055001
- Wolk, S. J., Günther, H. M., Poppenhaeger, K., et al. 2015, AJ, 150, 145
- Zechmeister, M., & Kürster, M. 2009, A&A, 496, 577